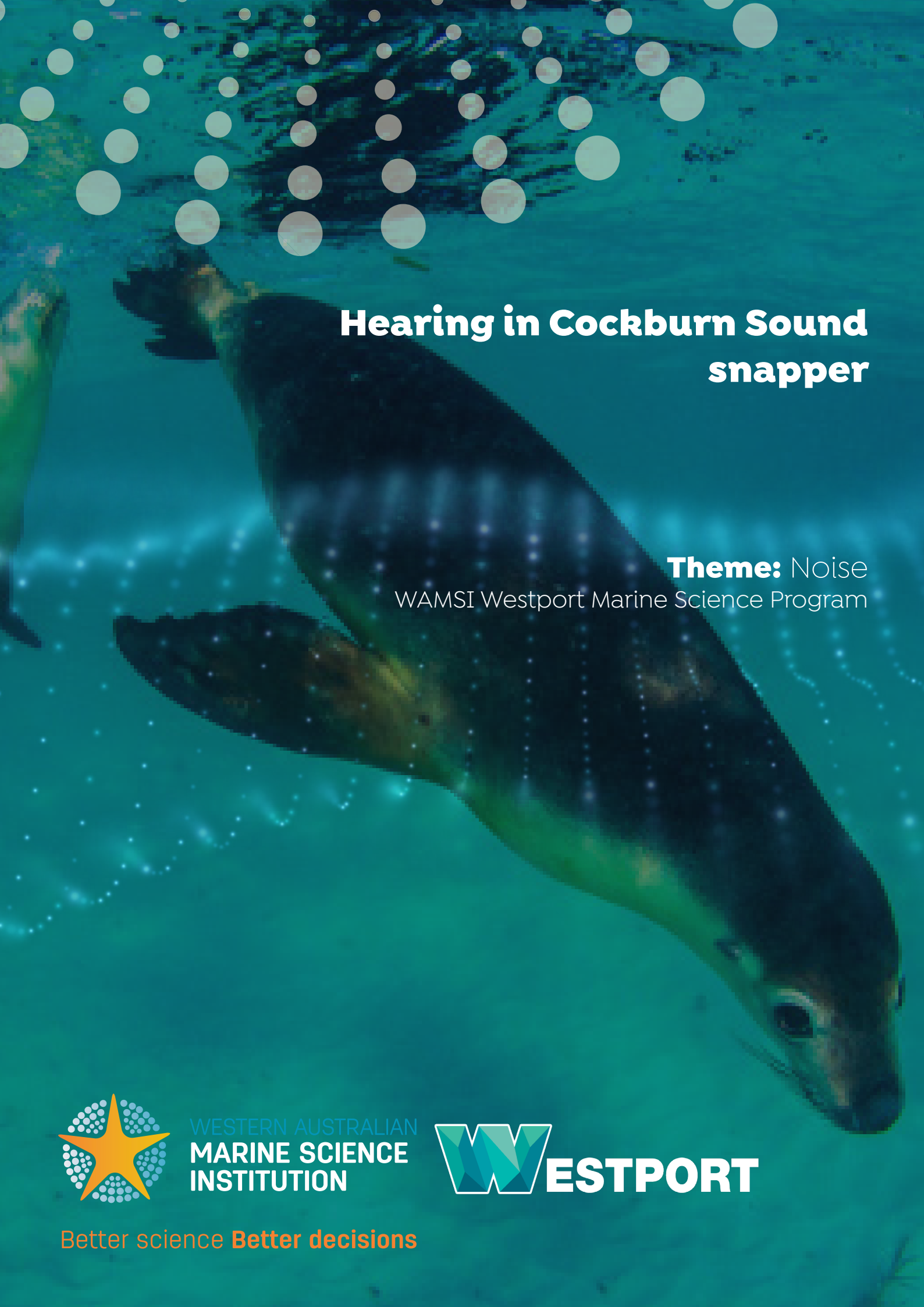

Hearing in Cockburn Sound snapper

Theme: Noise

WAMSI Westport Marine Science Program

WESTERN AUSTRALIAN MARINE SCIENCE INSTITUTION

WESTPORT

Better science **Better decisions**

WAMSI WESTPORT MARINE SCIENCE PROGRAM

WESTERN AUSTRALIAN MARINE SCIENCE INSTITUTION

WESTPORT

ABOUT THE MARINE SCIENCE PROGRAM

The WAMSI Westport Marine Science Program (WWMSP) is a $13.5 million body of marine research funded by the WA Government. The aims of the WWMSP are to increase knowledge of Cockburn Sound in areas that will inform the environmental impact assessment of the proposed Westport development and help to manage this important and heavily used marine area into the future. Westport is the State Government's program to move container trade from Fremantle to Kwinana, and includes a new container port and associated freight, road and rail, and logistics. The WWMSP comprises more than 30 research projects in the biological, physical and social sciences that are focused on the Cockburn Sound area. They are being delivered by more than 100 scientists from the WAMSI partnership and other organisations.

FUNDING SOURCES
The $13.5 million WAMSI Westport Marine Science Program was funded by the Western Australian Government, Department of Transport. WAMSI partners provided significant in-kind funding to the program to increase the value to >$22 million.

DATA
Finalised datasets will be released as open data, and data and/or metadata will be discoverable through Data WA and the Shared Land Information Platform (SLIP).

YEAR OF PUBLICATION
August 2025

This report is part of the project: Hearing sensitivity of Australian sea lions, little penguins and fish.

CITATION
Wei, C., Parsons, M., Erbe, C. (2025). Hearing in Cockburn Sound snapper. Prepared for the WAMSI Westport Marine Science Program. Western Australian Marine Science Institution, Perth, Western Australia. 26 pp.

FRONT COVER IMAGE
Theme: Noise

Contents

The WAMSI Westport Marine Science Program is a $13.5 million body of research that is designed to fill knowledge gaps relating to the Cockburn Sound region. It was developed with the objectives of improving the capacity to avoid, mitigate and offset environmental impacts of the proposed Westport container port development and increase the WA Government's ability to manage other pressures acting on Cockburn Sound into the future. Funding for the program has been provided by Westport (through the Department of Transport) and the science projects are being delivered by the Western Australian Marine Science Institution.

1 Title: Hearing in Cockburn Sound snapper (*Chrysophrus auratus*)

Author/s
Chong Wei, Centre for Marine Science and Technology, Curtin University; chong.wei@curtin.edu.au
Miles Parsons, Australian Institute of Marine Science; m.parsons@aims.gov.au
Christine Erbe, Centre for Marine Science and Technology, Curtin University; c.erbe@curtin.edu.au

Project
Curtin Project Number: RES 64481
CMST Project Number: 1594-5

Executive Summary

Underwater sound is an important sensory modality for fishes. However, as human activity in marine environments increases, so does the contribution of anthropogenic noise from sources such as vessels, pile driving, and seismic exploration. While the impacts of underwater noise on marine mammals are relatively well studied, fishes—many of which are ecologically significant, acoustically active, and vulnerable to disturbance—have received far less attention. This knowledge gap limits our ability to assess and mitigate the ecological consequences of noise pollution, particularly for species that underpin valuable fisheries.

Chrysophrys auratus, is a demersal sparid widely distributed across southern Australian and New Zealand waters. It occupies a broad range of habitats, exhibits strong site fidelity, and supports both commercial and recreational fisheries. Its long lifespan, benthic lifestyle, and regular exposure to noise from coastal developments make it a useful model species for investigating how fishes respond to underwater sound.

In this study, we applied finite element modelling (FEM) based on high-resolution microCT scans to examine the responses of the sagittal otolith—the snapper's primary hearing organ—to incident sound arriving from four directions: front, side, back, and top. We also developed 3D acoustic models from medical XCT scans of three snapper individuals of varying sizes and ages to simulate the sound reception process in the fish and investigate variation in hearing directionality and sensitivity.

The results revealed that otolith response is directionally dependent, with top-down sound generally inducing greater mechanical stimulation—suggesting a higher risk of damage to the hair cells on the macula located in the sulcus. We also observed inter-individual variation, including a reduction in peak response frequency and sensitivity with increasing body size (and likely age). This decline in auditory sensitivity may be associated with age-related changes (e.g., degeneration of sensory hair cells in the inner ear or reduced neural responsiveness), but is often attributed to cumulative noise exposure.

This imaging-based modelling approach offers an alternative to traditional hearing tests and contributes critical insights into the mechanisms of fish hearing. The outcomes of this study provide valuable data to inform environmental impact assessments and support the development of targeted noise mitigation strategies for commercially important fish species in Cockburn Sound and other noise-exposed marine habitats.

2 Introduction

Underwater sound is an important modality for marine fauna, including fishes, which both produce and receive information from acoustic cues. There are many types of fish sounds around Australia (Hawkins et al., 2024, 2025), including from commercially and ecologically important species that are distributed around the Perth area (Parsons et al., 2013a, 2013b), and over 100 species have had audiograms developed to characterise their sensitivity to sound (Wiernicki et al., 2020). Anthropogenic noise has become a pervasive pollutant in many marine environments, arising from commercial and recreational activities such as shipping, dredging, pile driving, and seismic exploration (Popper & Hawkins, 2018). While the impacts of underwater noise on marine mammals and the need to characterise their hearing sensitivity have received considerable attention, studies on fish have examined the effects of various noise sources, including impacts on early life stages such as eggs and larvae (Hastings et al., 1996; McCauley et al., 2003; Popper et al., 2005; Debusschere et al., 2016; Faria et al., 2022). However, compared to mammals, fish still remain comparatively understudied. This knowledge gap limits our ability to assess and mitigate the ecological consequences of acoustic disturbance on fish populations, including species of commercial and ecological significance (Popper et al., 2005).

Chrysophrys auratus, commonly known as 'snapper' in Australia (also referred to as Australasian snapper or pink snapper), is a demersal sparid, widely distributed across southern temperate waters of Australia and New Zealand (Fowler et al., 2017). The species inhabits a range of coastal and offshore environments from shallow bays to depths exceeding 200 m and plays a critical role in benthic ecosystems as both predator and prey. *C. auratus* is long-lived (up to ≈40 years) reaches a maximum length of approximately 1.3 m, and weight of over 20 kg, and exhibits strong site fidelity. In Cockburn Sound, this species forms spawning aggregations, and the area functions as a critical nursery habitat for juveniles during their first ~18 months of life. Notably, Cockburn Sound, Warnbro Sound, and Owen Anchorage are among the few locations between Kalbarri and Geographe Bay (WA) where both large adults (>70 cm total length, TL) and 0+ juveniles consistently occur (Breheny et al., 2012). This species supports one of Australia's most valuable commercial and recreational fisheries (Fowler et al., 2017). Its broad geographic distribution, ontogenetic habitat shifts, and exposure to noise from coastal developments and seismic surveys make it a useful model species for studying the effects of anthropogenic sound on fish auditory function.

Fishes detect sound primarily through their otolith organs, which function as inertial sensors. The dense otoliths are mechanically coupled to the hair cells of the macula via a gelatinous otolithic membrane. Differential motion between the otolith and macula, induced by sound waves, deflects the sensory hair bundles and generates neural impulses (Popper & Fay, 1999). In most teleosts (bony fishes), the saccular (sagittal) otolith is the principal auditory end organ, particularly sensitive to particle motion and low-frequency sound (Schulz-Mirbach et al., 2019). Previous studies have demonstrated that high-intensity acoustic exposure, such as air-gun pulses used in seismic surveys, can damage the hair cells of fish ears and impair auditory function. McCauley et al. (2003) observed significant macular damage following controlled air-gun exposure in pink snappers. However, subsequent experiments under different exposure conditions have produced inconsistent outcomes, raising questions about the role of additional influencing factors, including otolith geometry and the direction of sound incidence. To investigate these factors, recent studies by Wei and McCauley (2022, 2023) employed finite element (FE) modelling based on micro-computed tomography (microCT) of *Centroberyx gerrardi* (bight redfish). Their models simulated the response of saccular otoliths to sound arriving from horizontal and vertical directions. Results indicated that vertically incident sound induced greater differential motion and stress at the otolith-macula interface compared to horizontally incident sound, potentially increasing the risk of hair cell damage. These findings suggest that both directional exposure and otolith morphology are critical determinants of susceptibility to acoustic trauma.

Building on this framework, the present study applied FEM to *Chrysophrys auratus* to examine how the sagittal otolith responds to incident acoustic stimuli from different directions. First, using microCT-derived otolith data, we simulated otolith responses to sound arriving from four directions: front, side, back, and top. The resulting acceleration, displacement, and shear stress were calculated and compared. Second, using medical XCT-derived anatomical data from three *C. auratus* individuals of different ages and sizes, we simulated whole-head sound reception and extracted otolith motion parameters (e.g., acceleration) for inter-individual comparison.

This study contributes to a mechanistic understanding of directional and morphological influences on sound reception in fish. The findings offer important insights for improving noise impact assessments and inform conservation strategies for acoustically sensitive fish species in noise-affected habitats, particularly in Cockburn Sound—a biologically and economically important embayment that supports spawning aggregations and serves as a nursery for key fish species, but is also subject to intense anthropogenic activity such as dredging, shipping, and coastal development.

3 Materials and Methods

3.1 Specimen Collection and Medical CT scan

Fish were collected from the Cockburn Sound area by the Department of Primary Industries and Regional Development, provided through WWMSP Project 7.3 and donated after sampling (University of Western Australia, Animal Ethics Approval 2022ET422). Three male fish (TL :575, 645 and 710 mm, classed as small, medium and large, respectively; Fig 1A) underwent X-ray computed tomography (XCT) scanning shortly after being euthanised, to ensure the preservation of anatomical integrity and tissue freshness (Figures 1B and 1C).

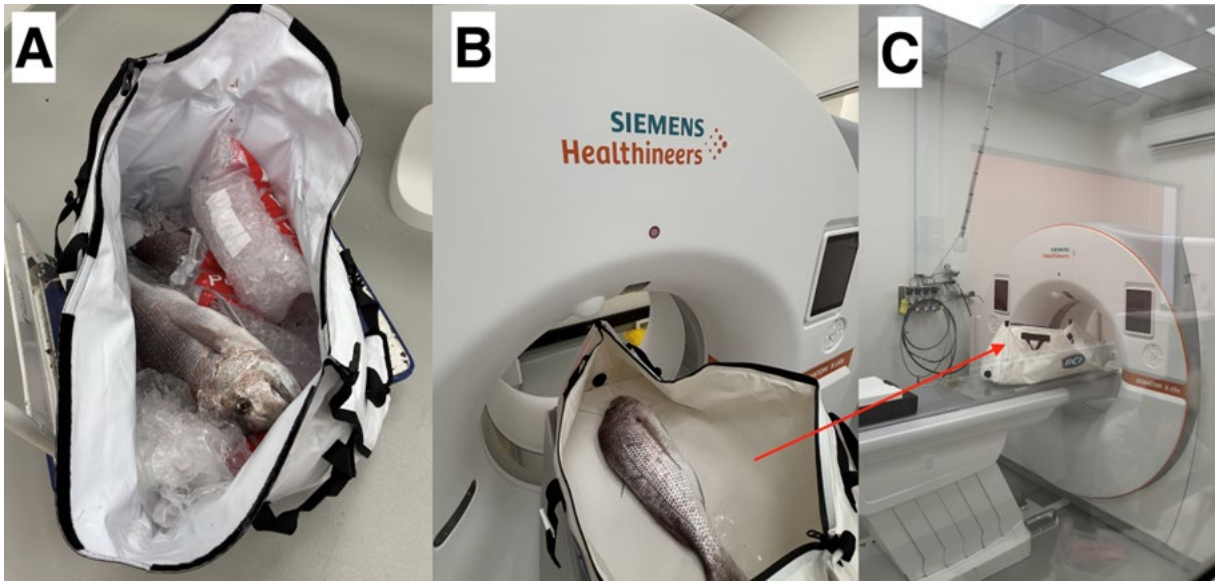

Figure 1. X-ray computed tomography scanning of the snappers. (A) Three collected snappers (full body). (B) XCT scan of one of the snappers. (C) XCT scan of a snapper in a fish bag.

Accurate FE modelling requires high-fidelity inputs of both geometry and material properties. As a first step, medical X-ray computed tomography (XCT) scanning was performed on all fish. XCT is a non-destructive technique that provides high-resolution 3D images, allowing detailed examination of internal anatomical structures without the need for dissection.

Whole-body XCT scans were conducted using a Siemens SOMATOM Definition AS medical scanner located at the Commonwealth Scientific and Industrial Research Organisation (CSIRO), Curtin Bentley (Figures 1B and 1C). This system enables rapid 3D scanning and produces transverse images at a resolution of 128 × 245 pixels. The scanner was calibrated using air and water, making it suitable for imaging organic materials. Scans were acquired using a 0.6 mm spiral acquisition and a slice increment of 0.1 mm. Beam energy was set to 100 kV and 500 mA to maximise phase contrast between tissues.

The voxel size (i.e. the three-dimensional pixel size) was configured to allow complete coverage of the fish head and was set to 380 µm × 380 µm × 100 µm. Two Siemens image reconstruction algorithms were applied. Both reconstructions were saved in DICOM format. The DICOM data were then imported into Horos™ (Horos Project, Geneva, Switzerland) for CT image analysis and 3D geometric model reconstruction (Figure 2). All structures were exported as stereolithography (STL) files after optimization and modification (i.e., smoothing, removing overlapping and self-intersections, etc.).

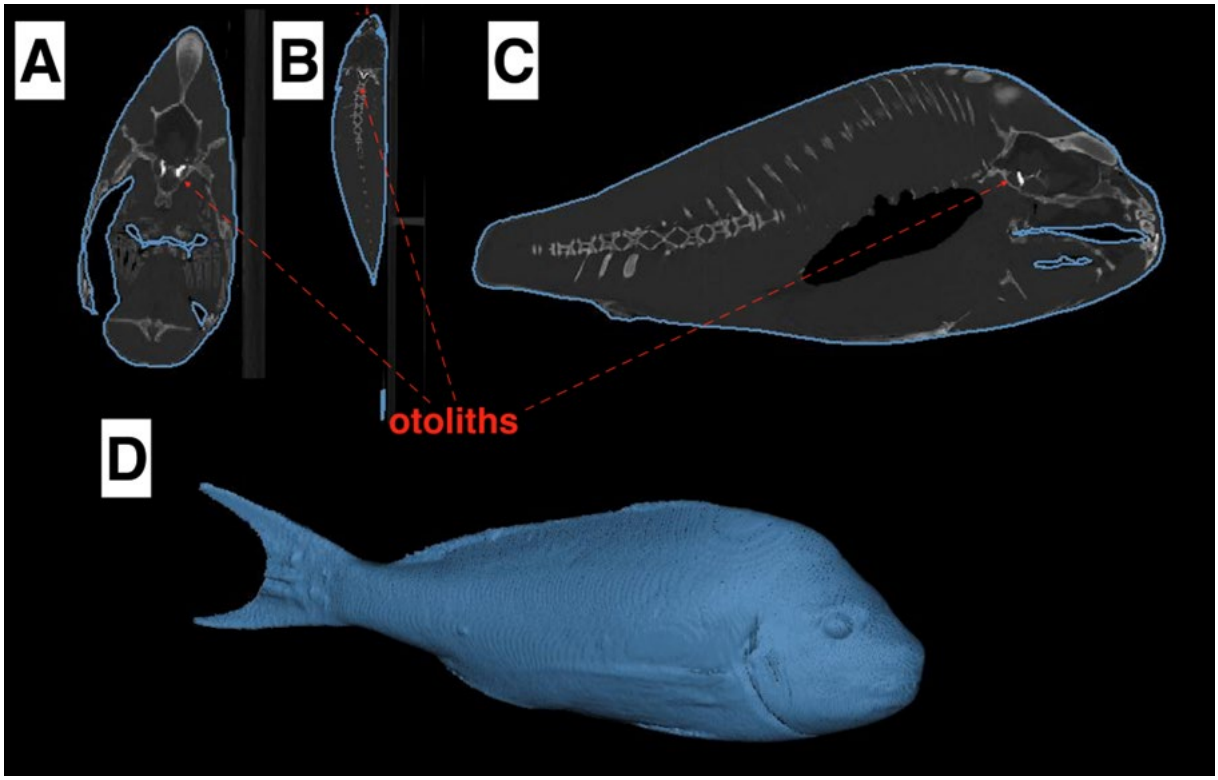

Figure 2. XCT scan of a whole snapper. (A) Cross plane, (B) frontal plane, and (C) sagittal plane of the head. (D) 3D reconstruction of the fish. The grey level represents the different HU values (Hounsfield Units), a dimensionless unit universally used in CT scanning express CT numbers in a standardized and convenient form. HU values are obtained from a linear transformation of the measured attenuation coefficients.

3.2 Dissection, MicroCT Scan and Data Analysis

To obtain high-resolution structural details of the otoliths, dissections were performed to carefully extract the otoliths along with the surrounding otic capsule (Figure 3A). The extracted structures were scanned separately at the Centre for Microscopy, Characterisation and Analysis (CMCA), University of Western Australia, and the X-ray Computed Tomography Facility at the John de Laeter Centre (JdLC), Curtin University. Each sample was securely placed inside a plastic container and mounted on a cylindrical stand to minimise movement during tomography data acquisition (Figure 3B).

One otolith sample was scanned at the CMCA using an Xradia VersaXRM-500 microCT scanner. The scan was conducted with an isotropic voxel size of 25 µm, using a power setting of 80 kV and 87 µA. A total of 1018 projections were collected over a 360° rotation, with an exposure time of two seconds per view. Cone-beam reconstruction was performed, and the resulting image stacks were saved in TIFF format. Two additional otolith samples were scanned at the JdLC using a Thermo Fisher Scientific HeliSCAN MicroCT Mk2 scanner. This system features a 160 kV transmission microfocus tube with a tungsten target and a high-resolution amorphous silicon flat-panel detector (3072 × 3072 pixels, 139 µm pixel size). Scans were conducted at 80 kV and 100 µA, with a 2 mm aluminium filter placed in front of the detector to reduce beam hardening artefacts. A space-filling acquisition trajectory was employed, enabling continuous, geometrically accurate 3D imaging of tall samples without stitching artefacts. The projections were reconstructed on a GPU cluster using an iterative method, producing digital 3D volumes with voxel sizes ranging from 25 to 30 µm, depending on sample size. All scan data were imported into Horos™ (Horos Project, Geneva, Switzerland) for 3D reconstruction and visualisation.

Bony fishes have two ears with three pairs of otoliths: utricular (lapillus) otoliths, lagenar (asteriscus) otoliths, and saccular (sagittal) otoliths. Figures 3C and D display the data analysis of the microCT data and 3D reconstruction of the otolith including these three parts. Otolith scans were exported as STL files after optimization and modification (i.e., smoothing, removing overlapping and self-intersections, etc.). The reconstructed geometry captured key morphological features of the saccular otoliths, including the cauda and ostium regions and the sulcal groove. After comparing otoliths from three specimens, the geometries were found to be similar. Therefore, one representative set was selected for later numerical modelling.

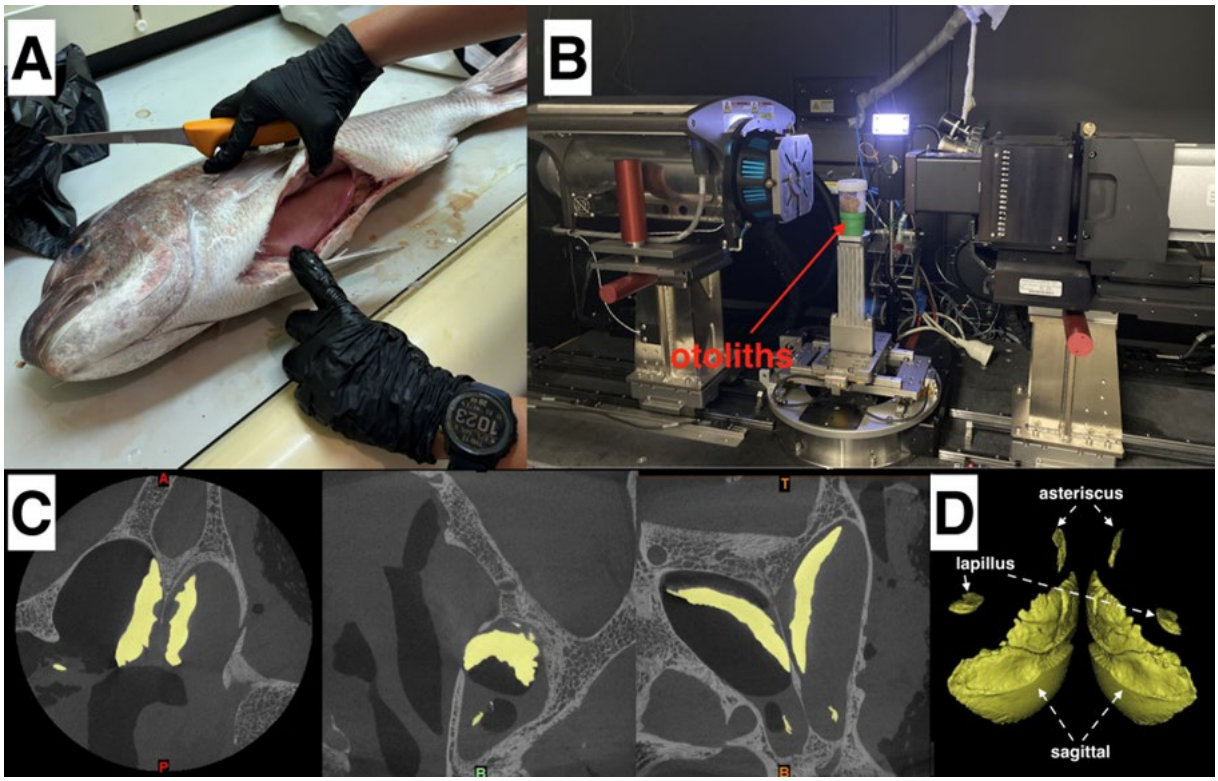

Figure 3. Dissection and microCT scanning. (A) Dissection of a snapper. (B) MicroCT scanning of an otolith. (C) Three views of microCT scan data. (D) Detailed 3D reconstruction of the otolith, including three pairs of otoliths.

3.3 Acoustic Property Measurement

After dissection to collect the otoliths, two epaxial muscles were obtained and labelled as No. 1 and No. 2 (Figure 4B). These muscle samples were first scanned using CT prior to acoustic property measurements. A 3D reconstruction of muscle No. 1 is shown in Figure 5C. All measurements were conducted at a controlled room temperature of 25 °C to minimise the influence of ambient temperature fluctuations on the results.

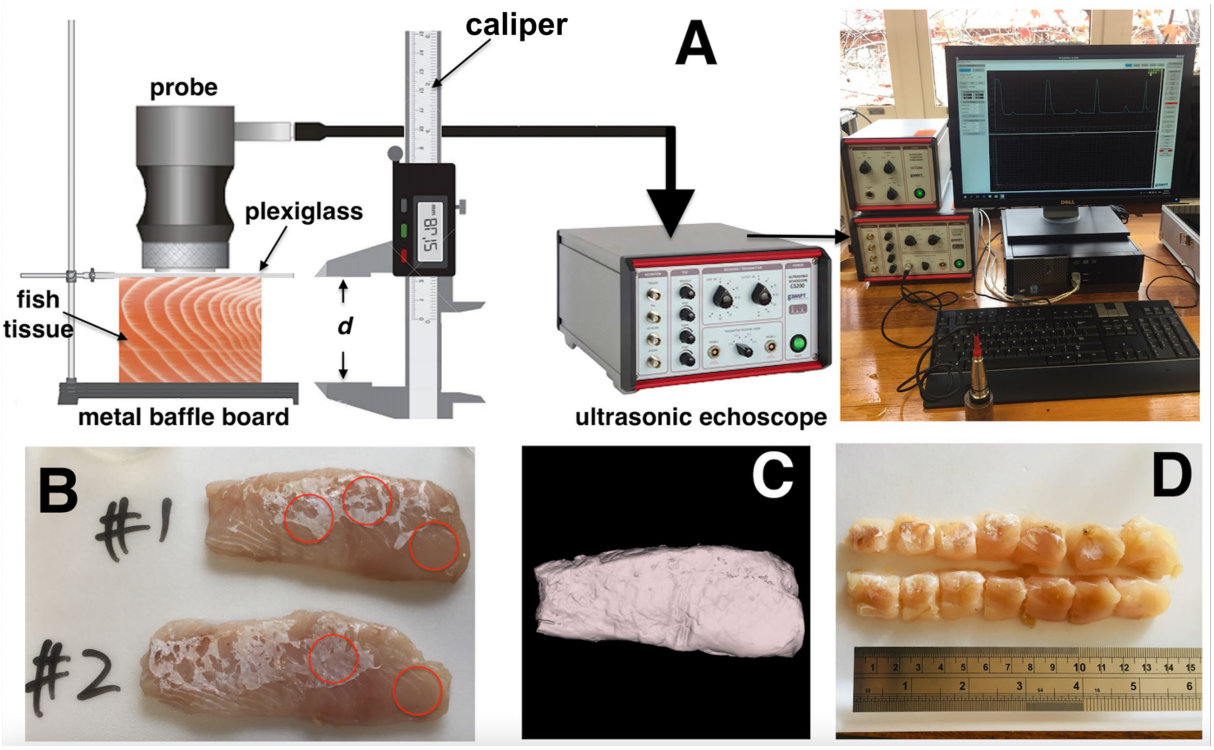

Figure 4. Tissue property measurement. (A) Custom-designed device for measuring sound speed in tissue. (B) Two epaxial muscles dissected from the fresh fish specimen. (C) 3D CT reconstruction of muscle No. 1. (D) Muscle samples segmented for density measurements.

Sound speed measurements of the epaxial muscles were conducted using a custom-designed apparatus (Figure 4A). Each muscle sample was placed naturally on a smooth metal baffle. A plexiglass sheet, aligned parallel to the metal board, was lowered gradually via a button-controlled mechanism. A GS200 echoscope was used to transmit ultrasound signals through the muscle, enabling precise measurement of sound transmission time. The GS200 is a high-resolution ultrasonic system that connects to a PC (Windows 7/8) via the GS-EchoView software (Figure 4A). An ultrasonic probe with a 25 mm diameter and robust snap-in connectors was used, capable of operating in transmitter/receiver mode or as separate transmitter and receiver units. Transmission and reception power could be adjusted as needed. Based on the muscle thickness, a 4 MHz signal frequency was selected to optimise the accuracy of time difference measurements. The circular markers in Figure 4B indicate the probe placement points.

When the ultrasound signal travelled through the muscle, part of the energy was reflected by the plexiglass surface (first reflected signal), while the remainder passed through the muscle and was reflected by the metal base (second reflected signal). The GS-EchoView software calculated the time difference ($\Delta t = t_2 - t_1$), where t_1 and t_2, represent the peak amplitudes of the first and second reflected signals, respectively. As the plexiglass was lowered to contact the muscle surface, the received signals could be viewed in real time on the computer. The muscle was gently compressed

(without noticeable deformation) between the plexiglass and the metal base until the signal amplitude peaked. A vernier calliper was then used to measure the distance d between the plexiglass and the metal baffle (Figure 4A). The total propagation distance was 2d, accounting for the forward and return travel of the signal through the muscle. This process was repeated at least five times for each probe position to obtain multiple measurements of both $\overline{\Delta t}$ and $\overline{d}$. No notable variation in travel time was observed across repetitions, indicating that tissue compression was unlikely to have affected the results. The average time difference ($\overline{\Delta t}$) and distance ($\overline{d}$) were then used to calculate the mean sound speed ($\bar{c}$) using the following formula:

$$\bar{c} = 2\bar{d}/\overline{\Delta t} \quad (1)$$

After the sound speed measurements, the epaxial muscles were immediately cut into several cubes. Only the larger, well-formed cubes that were cleanly cut were selected for further analysis (see Figure 4D). The mass of each muscle cube was measured using an electronic balance with an accuracy of 0.001 g. Each cube was weighed at least five times to obtain an average mass, $\overline{m}$. The volume of each muscle cube was determined via water displacement, following the method described in Wei et al. (2015). Each volume measurement was also repeated at least five times to obtain an average volume, $\overline{V}$. The average tissue density, $\bar{\rho}$, was then calculated using the following formula:

$$\bar{\rho} = \overline{m}/\bar{V} \quad (2)$$

Hounsfield unit (HU) values (CT information, which describes the CT numbers of the tissues, including bones, muscles, etc.) of each circled position in Figure 4B and each cube in Figure 4D can be respectively derived based on the CT scan data. Then, a univariate regression analysis was employed to obtain the linear regression equations of HU vs. sound speed and HU vs. density. Based on the two equations, the HU distribution exported from the CT scan data was converted to sound speed distribution and density distribution. The acoustic impedance distribution can be determined according to $Z_s = \rho c$, allowing the acoustic impedance model of the fish to be reconstructed.

The relationships between HU values, sound speed, and density of the fish tissues are presented in Figure 5. During volume measurements, small tissue fragments occasionally detached from some muscle cubes and remained in the measuring cylinder when the cubes were immersed in water. To ensure accuracy, these affected samples were excluded, and only the volume measurements of six intact cubes were retained for analysis. A linear correlation was observed between density and HU values, with a coefficient of determination (r^2) of 0.63. The linear regression equation is expressed as:

$$\rho = 1.5646 \frac{\mathrm{kg}}{\mathrm{m}^3} \times \overline{HU} + 968.1 \frac{\mathrm{kg}}{\mathrm{m}^3} \quad (3)$$

Some areas of the two epaxial muscles were either not flat enough at the bottom or not sufficiently thick; therefore, five suitable positions were selected for sound speed measurements. A linear correlation between sound speed and HU values was identified, with a coefficient of determination (r^2) of 0.79. The corresponding linear regression equation is:

$$c = 2.0908 \frac{\mathrm{m}}{\mathrm{s}} \times \overline{HU} + 1439.6 \frac{\mathrm{m}}{\mathrm{s}} \quad (4)$$

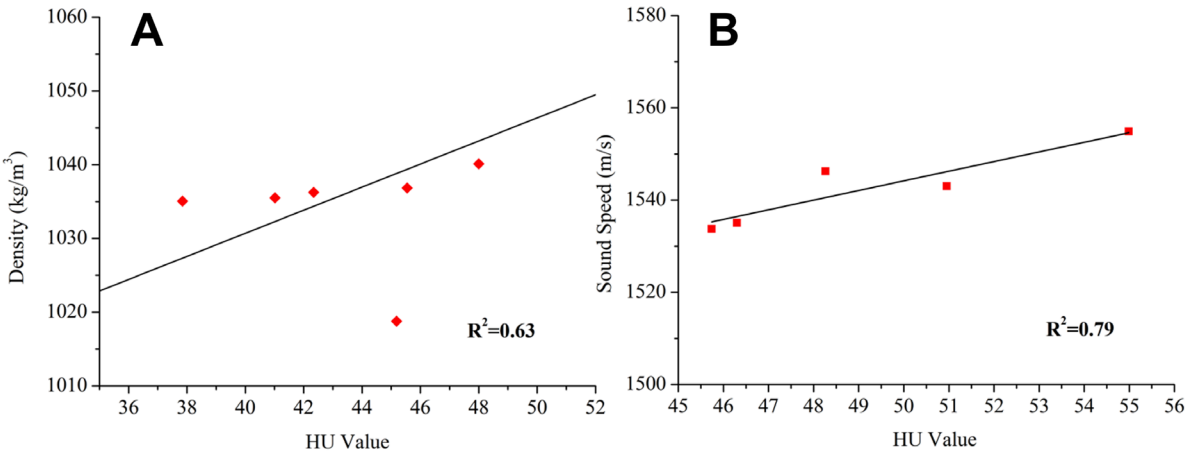

Figure 5 Regression analysis of HU values against tissue properties in fish: (A) HU vs. density, and (B) HU vs. sound speed.

Freese and Makow (1968) measured the acoustic properties of whitefish (*Coregonus dupeaformis*) tissues at 22°C. Shibata (1970) determined sound velocity and density of several fish species, including herring (*Clupea pallasii*), bigeye tuna (*Thunnus obesus*), yellow tail (*Seriola quinqueradiata*), common mackerel (*Pneumatophorus j. japonicus*), cod (*Anoplopoma fimbria*), salifin sandfish (*Arctoscopus japonicus*), wild-goldfish (*C. carassius* spp.*),* and sea trout (*Oncorhynchus gorbuscha*). The reported sound velocity and density in these fish species are shown in Table 1, ranging from 1,510–1,600 m/s and 1,040–1,090 kg/m³, respectively. In comparison, our reconstructed data ranged from 1,523–1,585 m/s and 1,030–1,061 kg/m³. Our results are qualitatively consistent with previous findings on the muscle properties of various fish species.

The acoustic properties of the entire fish body were reconstructed by converting the HU distribution into corresponding density and sound speed distributions using Equations 3 and 4. The resulting sound speed and density values of the snapper's epaxial muscles were then compared with previously reported data from other fish species, as summarised in Table 1.

Table 1. Acoustic properties of fish tissues

Fish species	Temperature (ºC)	Density (kg/m^3)	Sound speed (m/s)	Acoustic impedance (Pa·s/m^3)×10^6	Study
whitefish	22	1055	1549	1.63	Freese and Makow (1968)
herring	21	1050	1527	1.60	Shibata (1970)
bigeye tuna	18.3	1090	1600	1.74	Shibata (1970)
yellow tail	18.3	1063	1517	1.61	Shibata (1970)
common mackerel	18.3	1065	1539	1.64	Shibata (1970)
cod	18.3	1040	1510	1.57	Shibata (1970)
salifin sandfish	21	1045	1538	1.61	Shibata (1970)

wild-goldfish	22.3	1045	1529	1.60	Shibata (1970)
sea trout	19.5	1070	1543	1.65	Shibata (1970)
C. auratus	25	1030–1061	1523–1585	1.57–1.68	this study

3.4 Finite-Element Model Development

We developed detailed, anatomically accurate sound reception FE models based on high-resolution imaging data. These imaging-based FE modelling techniques enable us to predict audiograms and investigate sound reception mechanisms in *C. auratus*. Finite element analysis (FEA) is a numerical method for approximating solutions to boundary-value problems governed by partial differential equations. One of the key advantages of FEA is its capacity to handle complex geometries and provide high-resolution spatial information on anatomical structures, such as the fish head. These techniques have previously been employed to study sound reception and hearing in various marine species, including other fishes (Salas et al., 2019a, 2019b; Krysl et al., 2012; Wei and McCauley, 2022), baleen whales (Cranford and Krysl, 2015; Tubelli et al., 2012, 2018), and toothed whales (Aroyan, 2001).

The STL files were imported into COMSOL Multiphysics (Stockholm, Sweden) for FEA and subsequent data analysis. In this study, we developed two types of models: the “otolith-only” model and the “full-fish” model. For the otolith-only model, three pairs of otoliths were reconstructed from microCT data, with particular emphasis on the largest pair—the sagittal otoliths (Figure 6A). Incident sound was simulated from four directions: front, side, back, and top (Figure 6B), with each sound source positioned 2 cm from the otolith edges. For the full-fish model, the entire fish anatomy—including otoliths, bones, muscles, and swim bladder—was reconstructed from XCT data (Figure 6C). In this model, incident sound was simulated from the front, side, and top, with each sound source placed 8 cm from the outer edge of the fish body. The magnitude of the input pressure was arbitrary, as the model was linear. Stimuli were applied from each direction at selected frequencies, as indicated by the black arrows in Figures 6B and 6C. For the otolith-only model, the frequency was swept from 1 Hz to 8 kHz, with increments of 100 Hz. For the full-fish model, the frequency range was 10 Hz to 3 kHz, with increments of 20 Hz.

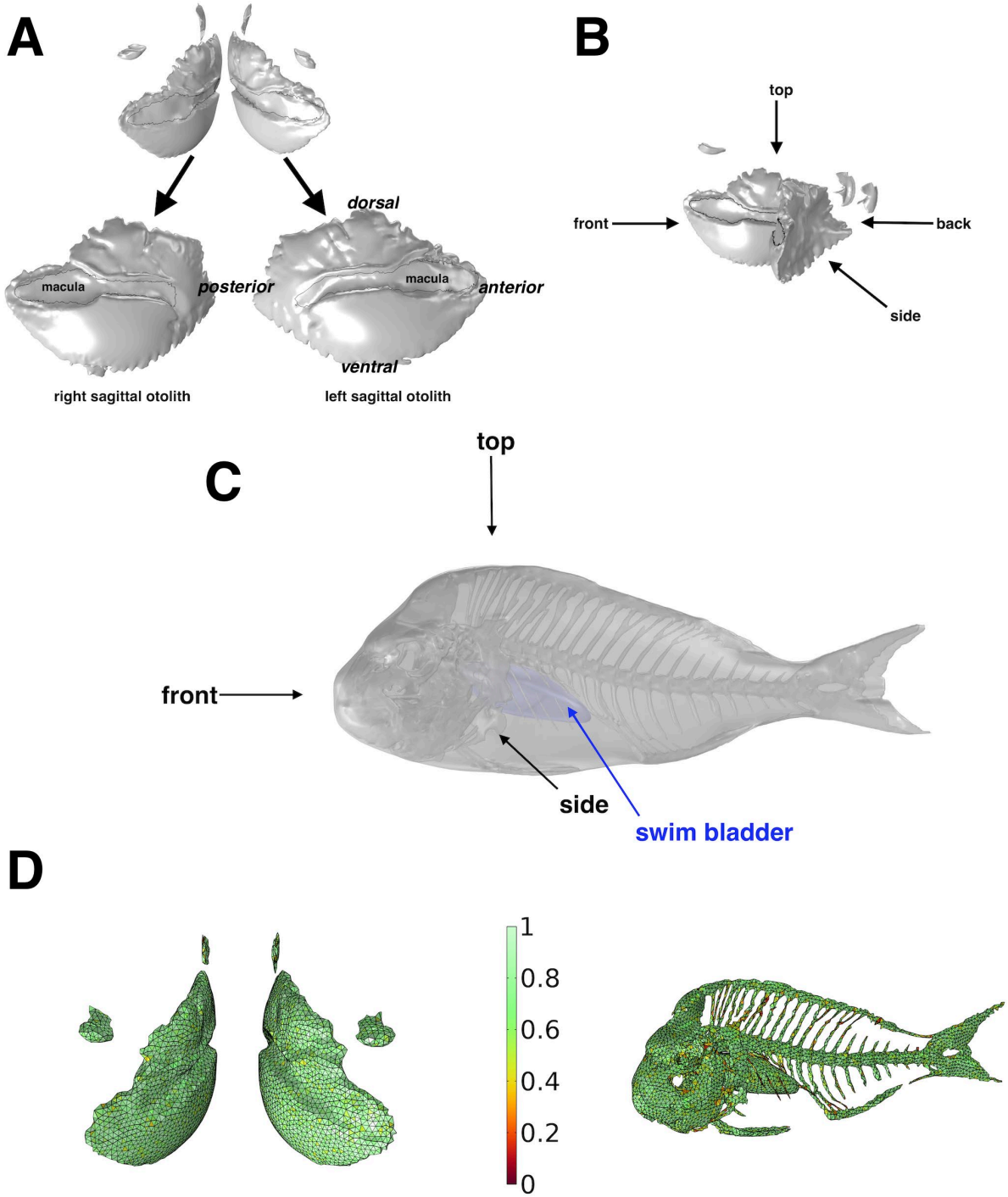

Figure 6. FE sound reception models of fish. (A) Two pairs of sagittal otoliths. (B) Setup of the otolith-only FE model constructed from microCT data. Black arrows indicate incident sound directions: front, side, back, and top. (C) Setup of the full-fish FE model based on XCT data. (D) Mesh quality of both model types. The colour scale represents mesh element quality, ranging from red (poor) to green (good). Mesh quality is a dimensionless metric between 0 and 1, where 1 indicates a perfectly regular element and 0 represents a degenerate element.

All models simulated the sound reception process from the surrounding water to the fish's otoliths. A water sphere was placed outside the fish body in both models to simulate acoustic transmission through water. A low-reflecting boundary condition (Bérenger, 1994) was applied to each sphere, allowing the simulation of sound propagation into free space with minimal boundary reflections.

COMSOL's built-in free mesher was used to generate a free tetrahedral mesh covering the entire model. This mesher automatically detects small features and narrow regions within the geometry and adjusts element sizes accordingly to accommodate fine structures and curved boundaries. It is widely accepted that element size in finite element-based acoustic simulations should be related to the wavelength of the propagated waves. A common practice is to define element sizes in terms of a fixed number of elements per wavelength. For 3D acoustic modelling, the general guideline is to apply at least 5–6 second-order elements per local wavelength to adequately resolve wave propagation, including elastic waves in solids (Thompson and Pinsky, 1994; Ihlenburg, 2006). In this study, the maximum mesh size was set to be no greater than one-sixth of the wavelength at each frequency for each material (e.g., water, muscle, bone). To ensure model accuracy, a mesh refinement or mesh convergence study was conducted by solving the model with progressively finer meshes to determine the optimal element size. Based on the results, we set 7.5 mm for all media for the otolith-only model, consisting of approximately 158,000 tetrahedral elements, resulting in 360,000 million degrees of freedom. For the full-fish model, the mesh was set as 1.3-30 mm for all media. The mesh contained approximately 363,000 tetrahedral elements, with 490,000 million degrees of freedom. Mesh quality is illustrated in Figure 6D.

The FE Pressure Acoustics-Frequency Domain module coupled with Solid Mechanics and an Acoustic-Structure Boundary was applied for the models. When acoustic waves propagate within the liquid medium, the longitudinal waves can be written as:

$$\frac{1}{\rho_0 c_s^2}\frac{\partial^2 p}{\partial t^2} + \nabla \cdot \left(-\frac{1}{\rho_0}\nabla p\right) = 0 \tag{5}$$

where p is the sound pressure, ρ_0 is the density (kg/m^3), and c_s is the speed of sound. The density ρ_0 is included in the equation because of its variations in different computational domains within the model. While the acoustic waves interact with the solid medium, such as the skull and ossicular chain, the longitudinal and transverse waves can be described as:

$$\rho\frac{\partial^2 \boldsymbol{u}}{\partial t^2} = (\lambda + 2\mu)\nabla(\nabla \cdot \boldsymbol{u}) - \mu\,\nabla \times (\nabla \times \boldsymbol{u}) \tag{6}$$

where $\boldsymbol{u}$ is the position vector, λ and μ are two Lame constants, characterizing compression and shear modulus in the solid medium, respectively (Urick, 1983). The boundary condition between solid and liquid media satisfies:

$$\boldsymbol{F} = -\boldsymbol{n}_s p \tag{7}$$

$$-\boldsymbol{n}_a \cdot \left(-\frac{1}{\rho_0}\nabla p\right) = \boldsymbol{a_n} \tag{8}$$

where $\boldsymbol{F}$ is the boundary load (force/unit area) on solid, $\boldsymbol{n}_s$ is the outward-pointing unit normal vector seen from inside the solid, p is the acoustic pressure, $\boldsymbol{n}_a$ is the outward-pointing unit normal vector seen from inside the liquid, ρ_0 is the density, and $\boldsymbol{a_n}$ is normal acceleration of the solid surface in the liquid domain boundary.

The following parameters were set for the models: (a) The sound speed in water surrounding the otoliths was set to 1483 m/s, with a density of 998 kg/m³. (b) The density and sound speed of the otoliths were 2970 kg/m³ and 3000 m/s, respectively (Schulz-Mirbach et al., 2018, 2019; Salas et al., 2019b; Campana and Thorrold, 2001). The Young's modulus of the otolith was set to 66 GPa (Ren et al., 2013), and the Poisson's ratio was 0.3, a value commonly used for bone (Tubelli et al., 2014). (c)

The sound speed and density of the fish muscle were set according to the acoustic property measurements described in Section 3.3.

3.5 Data Analysis

Sound pressure fields, displacement fields, and shear stress distributions were computed using COMSOL. The resulting sound pressure values were converted to decibel scale using the formula SPL = A + 20 $\log_{10}(P)$, where P is the normalised peak-to-peak sound pressure and A is a constant. These SPL values were only used to examine sound pressure levels on the otolith surfaces and are not intended to reflect decibel levels relevant to fish audiograms. To facilitate comparison of contour plots, the relative acceleration, displacement, and shear stress values were normalised to their respective maxima. The modelling data were subsequently exported from COMSOL for further analysis.

4 Results

When the incident sound arrived from the front, the acoustic stimulus travelled through the water and directly targeted the otoliths. While some fish species can detect sound pressure, all fish species are primarily detectors of particle motion, which can be expressed as acceleration and displacement (Popper and Hawkins, 2018). This motion is generated on the otolith and the coupled membrane as the otolith interacts with sound waves (Popper and Lu, 2000). Therefore, in addition to the sound pressure level (SPL), the motion (acceleration and displacement) and shear stress on both otoliths were computed at each excitation frequency, as shown in Figure 7. Figure 7 presents two examples of the results at 100 Hz and 500 Hz. The first row shows the SPL distribution on both sides of the otolith. The second row displays the relative acceleration (in colour) and displacement (indicated by arrows), while the third row illustrates the relative shear stress patterns on both sides of the otolith. It should be noted that all relative values in Figures 7–10 were normalised by dividing each result by its maximum value to enable clearer comparison.

The distributions of SPL, relative motion and shear stress on the left and right otoliths were roughly symmetrical, as the sound source was positioned at the centre, delivering approximately equal energy to both sides. Regions of higher SPL and motion were observed around the ostium, on the anterior side of the macula. Beyond this region of peak response, the magnitudes decreased along the posterior direction. The patterns observed at 100 Hz and 500 Hz were nearly identical.

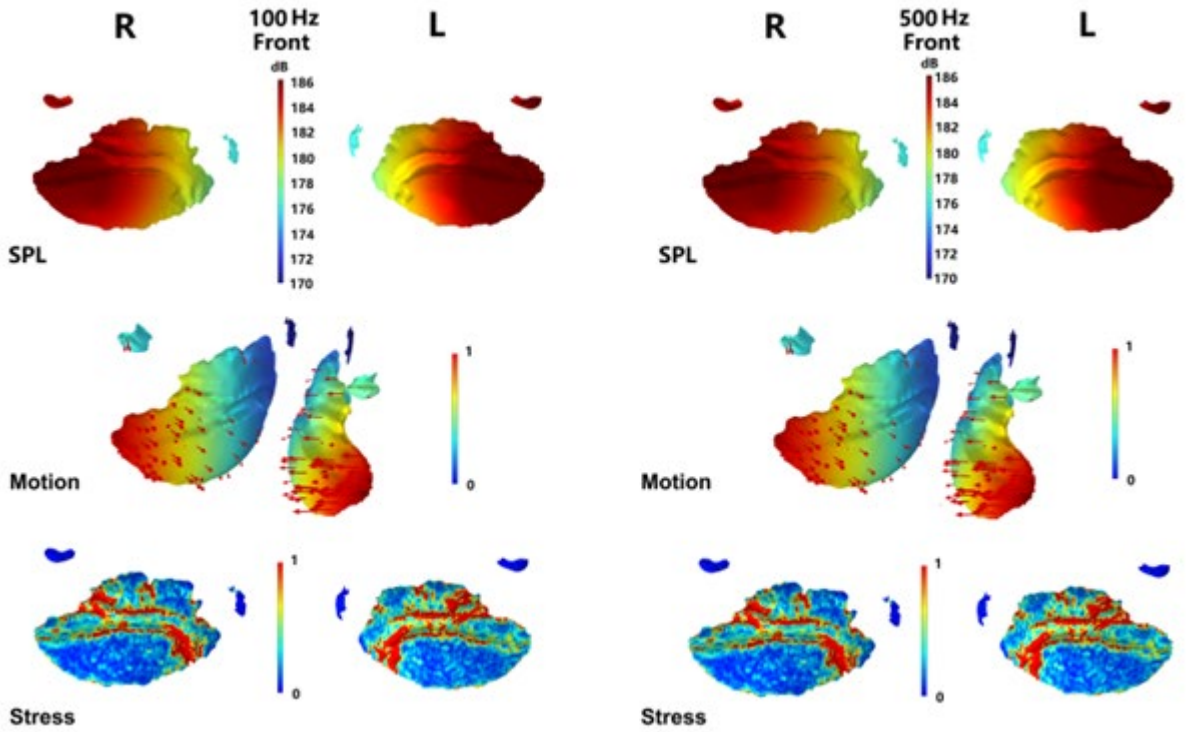

Figure 7. Sound pressure level, relative motion, and shear stress on the otolith surfaces at 100 Hz and 500 Hz, with incident sound arriving from the front. Colour scales represent SPL, relative acceleration, and shear stress, while red arrows indicate the magnitude and direction of displacement. To better illustrate displacement direction (red arrows), the otoliths in the second row are shown in their natural orientation.

When the incident sound arrived from the right-hand side, the acoustic stimulus travelled through the water and reached the right otolith first, followed by the left otolith. Figure 8 presents two examples of the results at 100 Hz and 500 Hz. The distributions of SPL, relative motion, and stress on the right and left otoliths were clearly asymmetrical. The values on the surface of the right otolith were significantly higher than those on the left, as the sound source was positioned closer to the right side. The patterns observed at 100 Hz and 500 Hz were nearly identical.

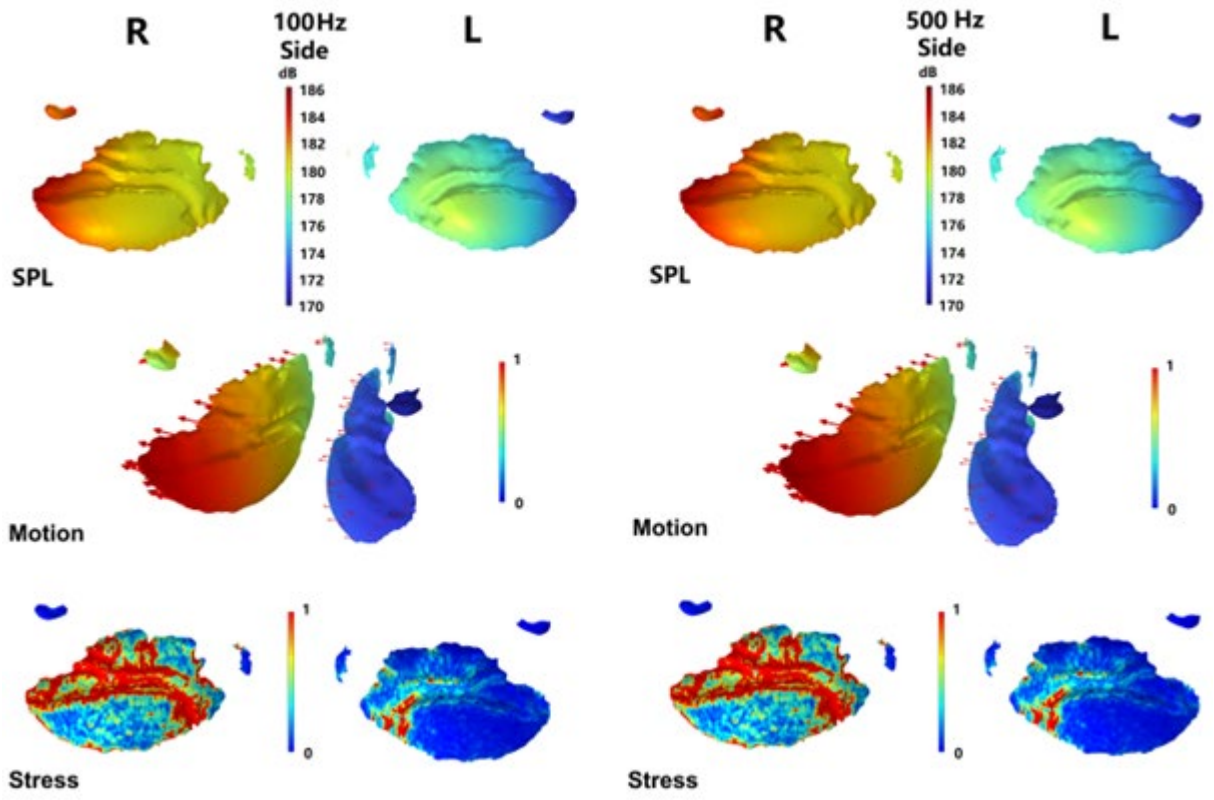

Figure 8. Sound pressure level, relative motion, and shear stress on the otolith surfaces at 100 Hz and 500 Hz, with incident sound arriving from the right-hand side. Colour scales represent SPL, relative acceleration, and shear stress, while red arrows indicate the magnitude and direction of displacement. To better illustrate displacement direction (red arrows), the otoliths in the second row are shown in their natural orientation.

When the incident sound arrived from the back, the acoustic stimulus travelled through the water and directly targeted the otoliths (Figure 9). The distributions of SPL, relative motion, and shear stress on the left and right otoliths were roughly symmetrical, as the sound source was positioned centrally at the back, delivering approximately equal energy to both sides—similar to the front case, but from the opposite direction. The SPL and motion on the surface of the asteriscus otoliths were significantly higher than those of the sagittal otoliths, as the asteriscus, located posteriorly, was closer to the sound source. The patterns observed at 100 Hz and 500 Hz were nearly identical.

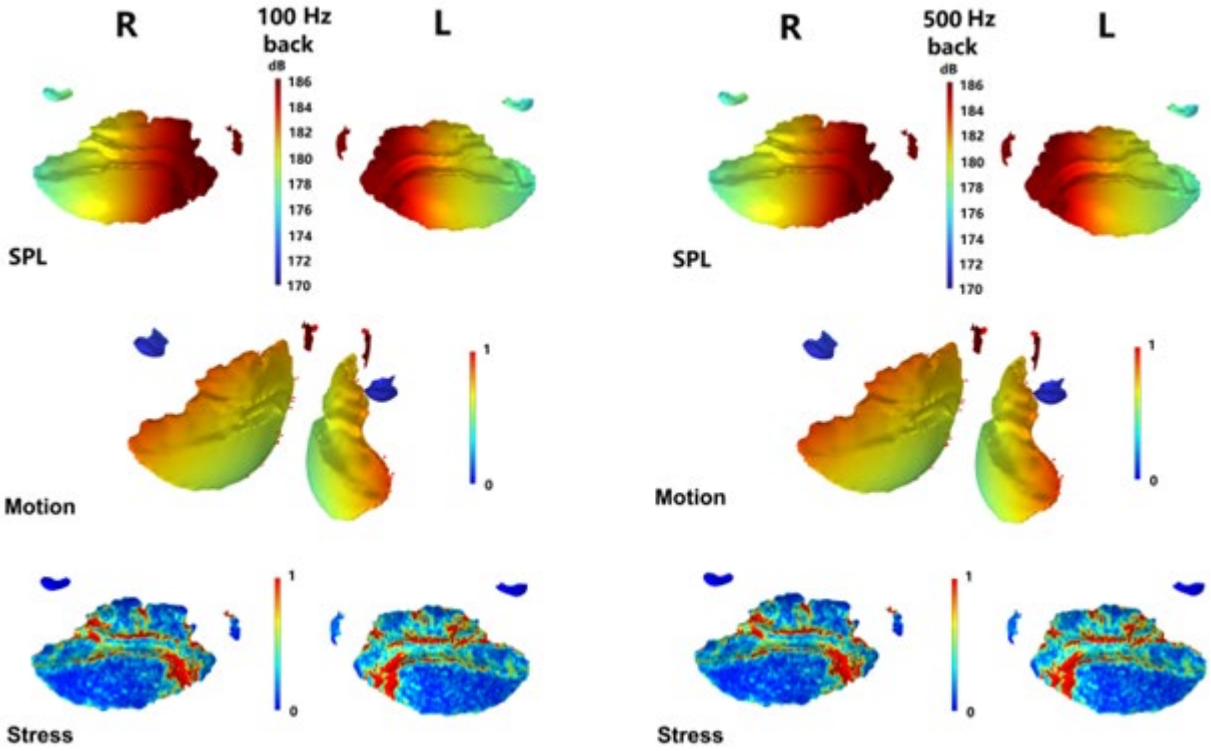

Figure 9. Sound pressure level, relative motion, and shear stress on the otolith surfaces at 100 Hz and 500 Hz, with incident sound arriving from the back. Colour scales represent SPL, relative acceleration, and shear stress, while red arrows indicate the magnitude and direction of displacement. To better illustrate displacement direction (red arrows), the otoliths in the second row are shown in their natural orientation. Note: The red arrows appear smaller in this figure because the overall displacement was lower when sound arrived from the back, compared to other directions.

When the incident sound arrived from the top, most of the acoustic energy was distributed on the lapillus otoliths and the dorsal side of the sagittal otoliths (Figure 10). The distributions of SPL, relative motion, and shear stress on the left and right otoliths were roughly symmetrical, as the sound source was positioned centrally above, delivering approximately equal energy to both sides. The SPL and motion on the surfaces of the lapillus otoliths and the dorsal side of the sagittal otoliths were significantly higher than those on the ventral side of the sagittal otoliths, due to their closer proximity to the sound source. The patterns observed at 100 Hz and 500 Hz were nearly identical.

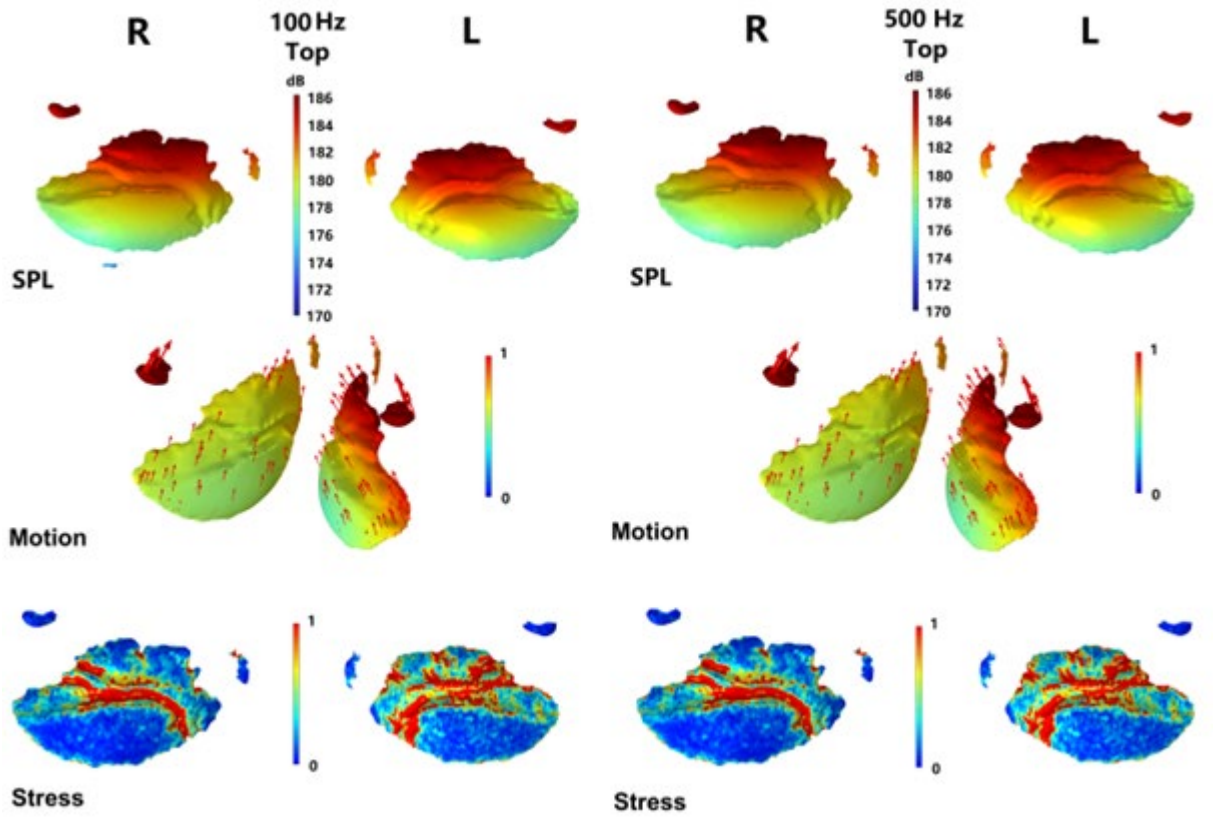

Figure 10. Sound pressure level, relative motion, and shear stress on the otolith surfaces at 100 Hz and 500 Hz, with incident sound arriving from the top. Colour scales represent SPL, relative acceleration, and shear stress, while red arrows indicate the magnitude and direction of displacement. To better illustrate displacement direction (red arrows), the otoliths in the second row are shown in their natural orientation.

Although the exact mechanisms of hearing in fish are not yet fully understood, research has demonstrated that the otolith organs play a key role in detecting particle motion, which is fundamental to hearing in all fish species. (Popper and Hawkins, 2018). Due to their high density, otoliths lag behind the motion of the macula when exposed to incident sound, due to their inertia (Dijkgraaf, 1960; Popper and Lu, 2000). This differential motion between the macula sacculi and the sagittal otolith leads to deflection of the hair cells (Popper and Fay, 1999), initiating the hearing process. As otolith-only models do not account for other anatomical structures such as the swim bladder, muscles, and bones, it is important to study otolith motion responses using a full-body model. This approach may provide essential insights directly related to hearing capability. Figure 11 shows comparisons of otolith acceleration across a frequency range of 1 Hz to 3 kHz for three fish of different sizes/ages, as well as the otolith acceleration responses of the small snapper to sounds from three different directions over the same frequency range.

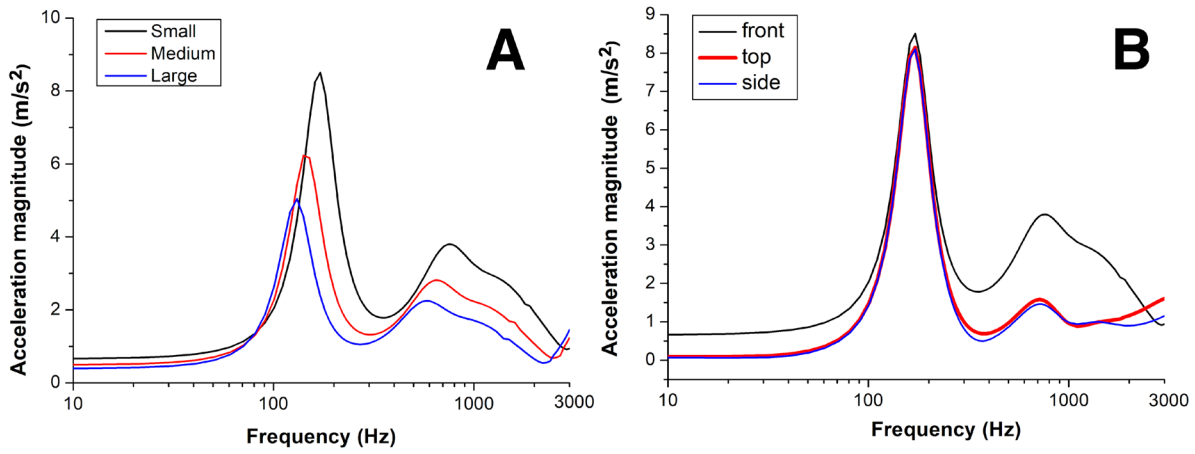

Figure 11 (A) Frequency response of otolith acceleration in three snappers of different sizes/ages. (B) Frequency response of otolith acceleration to incident sound arrivals from three directions (front, top, and side) in small-sized fish.

From Figure 11A, the general shapes of the curves were similar across the three fish. The peak otolith acceleration occurred at approximately 200 Hz for the small-sized fish, around 150 Hz for the medium-sized fish, and roughly 120 Hz for the large-sized fish. When incident sounds arrived from three different directions (front, top, and side) in the small-sized fish, the peak otolith acceleration was nearly the same (~200 Hz) across all three cases. However, the acceleration was slightly higher in the "front" case compared to the other two directions and displayed higher magnitudes of acceleration between 300 and 2000 Hz.

5 Discussion

5.1 Hearing Directivity

In the otolith-only models, distinct displacement patterns were observed under different sound incidence directions (Figures 7–10). First, the direction of otolith displacement was generally opposite to that of the acceleration. When sound arrived from the front or back, both otoliths displaced towards the midline of the fish (Figures 7, 9). When sound arrived from the right side, displacement was towards the right (Figure 8), and when sound came from top, displacement was directed dorsally (Figure 10). Second, the distribution of displacement varied depending on the direction of the incoming sound. For instance, when sound approached from the front, greater displacement was observed around the anterior region of the otoliths. In contrast, when sound came from the right, the right side of the otoliths showed greater displacement. These results suggest that the otoliths exhibited different "rocking" motions depending on the direction of the incident sound, indicating that different parts of the otolith moved differently. This finding aligns with the results of Wei and McCauley (2022; 2023), who modelled otolith motion and stress in bight redfish and linked it to potential hair cell damage. In addition, the distribution of SPL on the otoliths also varied with the direction of sound arrival (Figures 7–10). The different distribution and movement both across a single otolith and between the left and right otoliths in the pairs may be a mechanism for the fish to determine source direction. It should also be noted that sensitivity in the higher frequency range (300–3000 Hz) was greater in the front-incident case compared to the side or top cases. This likely reflects differences in sound reception pathways within the fish. When sound arrived from the front, motion was likely transmitted through dense cranial structures, such as the prominent bony hump on the forehead. In contrast, when sound came from the side or top, it did not travel directly through this bony structure; instead, part of the energy may have been reflected or scattered by the swim bladder.

5.2 Hearing Sensitivity

All three scanned *C. auratus* were adult males. However, due to differences in size (TL: 575 mm, 645 mm, and 710 mm), they were presumed to be of different ages. Given the relatively slow growth rate of *C. auratus*, with males typically reaching sexual maturity between 2–7 years and 220–560 mm (TL), and even later in the Perth region (5–6 years, 500–600 mm TL). Our modelling results suggest that the peak acceleration frequency remains largely unaffected by the direction of incoming sound. In contrast, the level and the frequency of the peak shifts with fish size (and likely therefore, age), indicating individual variation in hearing capability and a decrease in hearing through adulthood, with size. (There could be other underlying factors, such as innate differences in hearing sensitivity or prior exposure to environmental noise. Given the small sample size (n = 3), these factors cannot be ruled out, and more specimens are needed to clarify their effects.). Hearing sensitivity is thought to increase with age from juvenile to adulthood, presumably through the development of hair cells on the otoliths. When differences in hearing sensitivity among adults is observed, it is assumed that it is due to noise exposure and hair cell damage or degenerative changes. However, our data shows that such a decline in sensitivity and a downward shift in the most sensitive frequencies is partially due to fish size (likely with larger otoliths). Collecting and analysing younger (e.g., juveniles) and older specimens (which can grow up to 1300 mm TL) would be an important next step to further investigate ontogenetic changes in hearing ability. Juveniles are likely to be present in Cockburn Sound for up to ~18 months, and may differ in auditory sensitivity due to smaller otoliths and immature auditory structures. Additionally, larvae, also present in the area, may have limited hearing abilities or different frequency sensitivities, but further research is needed to clarify their auditory capabilities.

5.3 The Limitations of the Work

We acknowledge that the sample size used in the soft tissue analysis was relatively small; therefore, all data points, including the apparent outlier in Figure 5A, were retained in the regression analysis to

capture the full variability observed in the tissue measurements. This outlier may represent a muscle cube with slightly higher fat content, resulting in lower density and HU value, rather than reflecting a measurement error.

For the otolith-only model, the frequency was swept from 1 Hz to 8 kHz in increments of 100 Hz, resulting in a total of 80 datasets. As the results across frequencies appeared largely similar (see Figures 7–10), we chose to only present the results at 100 Hz and 500 Hz in these figures, considering the typical hearing sensitivities of fishes (Sand and Karlsen, 1986; Fay, 1988).

For marine mammals and birds, when incident sound enters the middle ear via the ear canal, it drives the stapes/columella footplate to vibrate, pushing in and out on the oval window of the cochlea (Cranford and Krysl, 2015; Frahnert et al., 2019; Wei et al., 2024). A transfer function between the input sound pressure and the resulting motion of the stapes/columella footplate (i.e., velocity) can be computed (Cranford and Krysl, 2015; Tubelli et al., 2012, 2018). In contrast, fish primarily detect sound through particle motion rather than pressure, and their exact hearing mechanism remains unclear—for instance, the extent to which they can sense sound pressure, i.e., how much the presence, volume, distance of the swim bladder to the otolith affects the motion of the otolith is still under investigation. Therefore, the methods previously used to predict hearing capabilities in Australian sea lions and little penguins (Wei et al., 2024) are unlikely to be suitable for fish. These curves, therefore, 1) are represented on a different scale to the dB scale used to represent hearing and so need a scaling factor; and 2) require an anchor with which to fix this relative curve to a threshold level of hearing. Further, hearing sensitivity is dependent on the number of hair cells that can detect otolith movement, a component not measured by this method. The current frequency response curves for fish therefore represent a relative sensitivity response that does not account for any changes due to an individual's life-history, such as noise exposure, unless it is directly measured for that individual. Further research with increased sample size will be necessary for a proof of concept on how to account for these factors. Nevertheless, the model developed in this study provides a valuable tool to examine potential auditory damage caused by intense noise from different directions, as well as to identify the frequency ranges to which fish otoliths are likely to be more sensitive.

5.4 Potential Effects of Anthropogenic Noise on *C. auratus*

5.4.1 Potential hair cell damage

Our force analysis (Figures 7–10) showed that the stress exerted on the otolith surface varied depending on the direction of incoming sound. The stress distribution for front-arriving sound (Figure 7) was similar to that for rear-arriving sound (Figure 9). In contrast, sound arriving from the top resulted in significantly higher stress concentrations in the cauda region (the narrow end of the macula groove) of both otoliths (Figure 10). These results align well with the spatial mapping of hair cell damage observed in a previous exposure experiment (Figure 5b in McCauley et al., 2003), where the majority of damage was concentrated in the cauda region when fish were exposed to impulsive air gun signals, from above. Our findings are also consistent with earlier modelling studies on *C. gerrardi* (Wei and McCauley, 2022, 2023), which share similar otolith geometry with *C. auratus*. In *C. auratus*, the otolith groove appears deep and narrow in the top view, but shallow and elongated in the front view. Due to this morphological configuration, sound waves arriving from the front or back are less likely to push the membrane against the sulcal groove edges, as there is more room for displacement. In contrast, when sound arrives from above, there is limited space for membrane movement, causing it to press directly against the inside of the sulcal groove and leading to higher localised stress. Therefore, our results suggest that fish with this type of otolith morphology may be more tolerant of horizontally arriving sound energy (front or back) than vertically arriving sound (from top). It should be noted, however, that these results are likely species-specific—fish with differently shaped otoliths may exhibit different, or even opposite, responses (Smith et al., 2022). Furthermore, sound energy is also likely to have age-specific effects, with different consequences across life stages such as eggs, larvae, juveniles, and adults. This study focused only on adult specimens; eggs, larvae, and juveniles were not included

due to challenges. As such, the findings may not reflect auditory sensitivity across these earlier developmental stages.

It also should be noted that the damage mechanisms discussed above are primarily associated with impulsive signals, such as those produced by pile driving and underwater explosions. While these types of activities are likely to occur during the construction of Westport, they are not expected to represent the dominant sound sources over the full duration of the project. When they do occur, their timing could potentially be managed to avoid sensitive ecological periods, such as *C. auratus* spawning. The more significant potential impact on C. auratus populations in Cockburn Sound arises from continuous noise sources, such as vessels and long-term dredging operations, particularly given that the area supports not only spawning aggregations but also serves as a nursery habitat for juveniles for up to ~18 months. A more detailed analysis of the effects of these continuous sources and the potential implications for the proposed container port construction is provided in the partner report on Project 7.3 (Parsons et al., 2025).

5.4.2 Potential noise sources

The modelling results presented here indicate that the fish otolith responds most strongly to sounds in the 150–200 Hz frequency range. Notably, this range overlaps with several common anthropogenic underwater noise sources. For example, ship traffic—a dominant source of ocean noise—produces sound primarily between 20 and 1000 Hz (Urick, 1983). Pile driving, frequently used in coastal construction, generates broadband acoustic energy between 50 Hz and 5 kHz (Erbe, 2009). Given the overlap in frequency, it is likely that *C. auratus* can detect these anthropogenic sounds. Such exposure may elicit behavioural changes or even lead to temporary threshold shifts (TTS) in hearing sensitivity (Popper and Clarke, 1976; Popper et al., 2005).

6 Conclusions/Recommendations

This is the first study using imaging-based FE modelling to investigate hearing in *C. auratus*. The results provide valuable insight into the frequency ranges that these fish are likely able to detect. Additionally, the findings suggest directional sensitivity in fish hearing—an important aspect that has been largely overlooked in previous research. Further, we observed a decline in sensitivity and frequency of peak response with increasing fish size, suggesting a possible decline in hearing sensitivity with age, once hair cell development has concluded. Such decline is often associated and attributed to noise exposure. This study, for the first time, provides an alternative or synergistic mechanism for that decline. The study also introduces a useful tool to assess potential damage to the coupled hair cells on the macula lying in the sulcus caused by sound arriving from different directions. Ultimately, this work contributes critical knowledge for marine conservation efforts. The outcomes can support the development of noise impact mitigation strategies and inform conservation management practices. For example, identifying the most sensitive hearing frequency range can help guide the timing and type of noise-generating activities (e.g., vessel operations and dredging) to avoid overlap with biologically important periods such as spawning.

7 References

Aroyan JL (2001) Three-dimensional modeling of hearing in *Delphinus delphis*. J Acoust Soc Am 110(6): 3305–3318.

Bérenger JP (1994) A perfectly matched layer for the absorption of electromagnetic waves. J Comput Phys 114(2): 185–200.

Breheny NB, Beckley LE, Wakefield CB (2012) Ichthyoplankton assemblages associated with pink snapper (*Pagrus auratus*) spawning aggregations in coastal embayments of southwestern Australia. J R Soc West Aust 95: 103–114.

Campana SE, Thorrold SR (2001) Otoliths, increments, and elements: Keys to a comprehensive understanding of fish populations? Can J Fish Aquat Sci 58, 30–38.

Cranford TW, Krysl P (2015) Fin whale sound reception mechanisms: Skull vibration enables low-frequency hearing. PLoS ONE 10(1): Article e0116222.

Debusschere E, Hostens K, Vanaverbeke J, Vandendriessche S, Van Ginderdeuren K, Vandecasteele B, Vincx M, Degraer S (2016) Effects of offshore wind farms on the early life stages of *Dicentrarchus labrax*, in The Effects of Noise on Aquatic Life II, edited by AN Popper and A Hawkins (Springer, New York), pp. 245–252.

Dijkgraaf S (1960) Hearing in bony fishes. Proc R Soc Lond Ser B 152:51–54.

Erbe C (2009) Underwater noise from pile driving in Moreton Bay, Qld. Acoust Aust 37(3): 87–92

Erbe C, King AR (2009) Modelling cumulative sound exposure around marine seismic surveys. J Acoust Soc Am 125(4): 2443–2451.

Fowler AJ, Huveneers C, Lloyd MT (2017) Insights into movement behaviour of snapper (*Chrysophrys auratus, Sparidae*) from a large acoustic array. Mar Freshw Res 68, 1438-1453.

Faria A, Fonseca PJ, Vieira M, Alves LMF, Lemos MFL, Novais SC, Matos AB, Vieira D, Amorim MCP (2022) Boat noise impacts early life stages in the Lusitanian toadfish: A field experiment. Sci Total Environ 811: 152278.

Fay RR (1988). Hearing in Vertebrates: A Psychophysics Databook (Hill-Fay, Winnetka, IL).

Frahnert S, Lindner M, Bendel E, Frahnert KH, Westphal N, Dahne M (2019) 3D-Visualization of the Ear Morphology of Penguins (*Spheniscidae*): Implications for Hearing Abilities in Air and Underwater. Proc Mtgs Acoust 37: 010018.

Freese M, Makow D (1968) High-frequency ultrasonic properties of freshwater fish tissue. J Acoust Soc Am 44(5):1282-9.

Hastings MC, Popper AN, Finneran JJ, Lanford PJ (1996) Effect of low-frequency underwater sound on hair cells of the inner ear and lateral line of the teleost fish *Astronotus ocellatus*. J Acoust Soc Am 99: 1759–1766.

Hawkins LA, Saunders BJ, Landero FMM, McCauley RD, Parnum IM, Parsons MJ, Erbe C (2023) Habitat type drives the spatial distribution of Australian fish chorus diversity. J Acoust Soc Am 154(4), 2305-2320.

Hawkins LA, Erbe C, Becker A, Browne CE, McCordic J, McWiliam J, McCauley RD (2024) The Australian fish chorus catalogue (2005–2023). Frontiers in Remote Sensing, 5, 1473168.

Ihlenburg F (2006) Finite element analysis of acoustic scattering (Springer Science, Business Media).

Krysl P, Hawkins AD, Schilt C, Cranford TW (2012) Angular oscillation of solid scatterers in response to progressive planar acoustic waves: Do fish otoliths rock? PLoS One 7, e42591.

McCauley RD, Fewtrell J, Popper AN (2003) High intensity anthropogenic sound damages fish ears. J Acoust Soc Am 113, 638–642.

Parsons MJ, McCauley RD, Mackie MC (2013) Characterisation of mulloway *Argyrosomus japonicus* advertisement sounds. Acoust Aust 41(3).

Parsons MJ, Longbottom S, Lewis P, McCauley RD, Fairclough DV (2013) Sound production by the West Australian dhufish (*Glaucosoma hebraicum*). J Acoust Soc Am 134(4), 2701-2709.

Popper AN, Clarke NL (1976) The auditory system of the goldfish (*Carassius auratus*): Effects of intense acoustic stimulation. Comp. Biochem Physiol 53, 11–18.

Popper AN, Hawkins AD (2018) The importance of particle motion to fishes and invertebrates. J Acoust Soc Am 143, 470–486.
Popper AN, Smith ME, Cott PA, Hanna WB, MacGillivray AO, Austin ME, Mann DA (2005) Effects of exposure to seismic air-gun use on hearing of three fish species. J Acoust Soc Am 117, 3958–3971.
Popper AN, Lu Z (2000) Structure–function relationships in fish otolith organs Fish Res 46, 15–25.
Popper AN, Fay RR (1999) The auditory periphery, in fishes in Comparative Hearing: Fish and Amphibians, edited by RR Fay and AN Popper (Springer-Verlag, New York), pp. 43–100.
Ren D, Gao Y, Feng Q (2013) Comparative study on nanomechanics and thermodynamics of fish otoliths Mater Sci Eng C 33(1), 9–14.
Salas AK, Wilson PS, Fuiman LA (2019a) Vibration of otolith-like scatterers due to low frequency harmonic wave excitation in water. Proc Mtgs Acoust 37, 010006.
Salas AK, Wilson PS, Fuiman LA (2019b) Ontogenetic change in predicted acoustic pressure sensitivity in larval red drum (*Sciaenops ocellatus*). J Exp Biol 222, jeb201962.
Sand O, Karlsen HE (1986) Detection of infrasound by the Atlantic cod J Exp Biol 125, 197–204.
Schulz-Mirbach T, Ladich F, Plath M, Heß M (2019) Enigmatic ear stones: What we know about the functional role and evolution of fish otoliths. Biol Rev 94, 457–482.
Schulz-Mirbach T, Olbinado M, Rack A, Mittone A, Bravin A, Melzer RR, Ladich F, Heß M (2018) In-situ visualization of sound-induced otolith motion using hard X-ray phase contrast imaging. Sci Rep 8, 3121.
Smith ME, Accomando AW, Bowman V, Casper BM, Dahl PH, Jenkins AK, Kotecki S, Popper AN (2022) Physical effects of sound exposure from underwater explosions on Pacific mackerel (*Scomber japonicus*): effects on the inner ear. J Acoust Soc Am 152(2):733–744.
Thompson LL, Pinsky PM (1994) Complex wave number Fourier analysis of the p-version finite element method. Comput Mech 13: 255–275.
Tubelli AA, Zosuls A, Ketten DR, Mountain DC (2018) A model and experimental approach to the middle ear transfer function related to hearing in the humpback whale (*Megaptera novaeangliae*). J Acoust Soc Am 144(2): 525–535.
Tubelli AA, Zosuls A, Ketten DR, Mountain DC (2014) Elastic modulus of cetacean auditory ossicles. Anatom Rec 297(5): 892–900.
Tubelli AA, Zosuls A, Ketten DR, Yamato M, Mountain DC (2012) A prediction of the minke whale (*Balaenoptera acutorostrata*) middle-ear transfer function. J Acoust Soc Am 132(5): 3263–3272.
Urick RJ (1983) Principles of Underwater Sound. McGraw-Hill, New York, pp. 1–423.
Wei C, McCauley RD (2022) Numerical modeling of the impacts of acoustic stimulus on fish otoliths from two directions. J Acoust Soc Am 152(6), 3226–3234.
Wei C, McCauley RD (2023) Finite element modeling of effects of acoustic stimulation on fish otoliths. I. AN Popper, J Sisneros, A Hawkins, and F Thomsen (Eds.), The effects of noise on aquatic life: Principles and practical considerations (pp. 1–15). Springer, Cham.
Wei C, Wang ZT, Song ZC, Wang KX, Wang D, Au WWL, Zhang Y (2015) Acoustic property reconstruction of a Yangtze finless porpoise's (*Neophocaena asiaeorientalis asiaeorientalis*) head based on CT imaging. PLoS ONE 10(4), e0121442.
Wei C, Erbe C (2024) Sound reception and hearing capabilities in the Little Penguin (*Eudyptula minor*): First predicted in-air and underwater audiograms. R Soc Open Sci, 11.
Wiernicki CJ, Liang D, Bailey H, Secor DH (2020) The effect of swim bladder presence and morphology on sound frequency detection for fishes. Rev Fish Sci Aquat 28(4), 459-477.

Submitted as draft	04/04/2025
Reviewed completed	27/06/2025
Submitted as revised draft	11/07/2025
Approved by Science Program Leadership team	30/07/2025
Approved by WAMSI CEO	07/08/2025
Final Report	12/08/2025

WESTERN AUSTRALIAN
MARINE SCIENCE
INSTITUTION